

## Highlights

### **A Multimodal Data Fusion Generative Adversarial Network for Real Time Underwater Sound Speed Field Construction**

Wei Huang, Yuqiang Huang, Yanan Wu, Tianhe Xu, Junting Wang, Hao Zhang

- A MDF-RAGAN model that quickly obtain sound velocity distribution without the need for underwater on-site data measurement.
- A residual block that makes the model learn the influence of SST on the variation of sound velocity.
- Embedded attention mechanism that makes the model learn the correlation of sound velocity distribution in large-scale spatial regions.

# A Multimodal Data Fusion Generative Adversarial Network for Real Time Underwater Sound Speed Field Construction

Wei Huang<sup>a</sup>, Yuqiang Huang<sup>a</sup>, Yanan Wu<sup>a,\*</sup>, Tianhe Xu<sup>b,\*</sup>, Junting Wang<sup>b</sup>,  
Hao Zhang<sup>a</sup>

<sup>a</sup>*Faculty of Information Science and Engineering, Ocean University of China, No.238  
Songling Road, Qingdao, 266100, Shandong, China*

<sup>b</sup>*School of Space Science and Technology, Shandong University (Weihai), No.180  
Wenhua West Road, Weihai, 264209, Shandong, China*

---

## Abstract

Sound speed profiles (SSPs) are essential parameters underwater that affects the propagation mode of underwater signals and has a critical impact on the energy efficiency of underwater acoustic communication and accuracy of underwater acoustic positioning. Traditionally, SSPs can be obtained by matching field processing (MFP), compressive sensing (CS), and deep learning (DL) methods. However, existing methods mainly rely on on-site underwater sonar observation data, which put forward strict requirements on the deployment of sonar observation systems. To achieve high-precision estimation of sound velocity distribution in a given sea area without on-site underwater data measurement, we propose a multi-modal data-fusion generative adversarial network model with residual attention block (MDF-RAGAN) for SSP construction. To improve the model's ability for capturing global spatial feature correlations, we embedded the attention mechanisms, and use residual modules for deeply capturing small disturbances in the deep ocean sound velocity distribution caused by changes of SST. Experimen-

---

\*Corresponding Author; Wei Huang and Yuqiang Huang contributed equally to this work.

*Email addresses:* hw@ouc.edu.cn (Wei Huang), yqhuang@stu.ouc.edu.cn (Yuqiang Huang), wuyan@ouc.edu.cn (Yanan Wu), thxu@sdu.edu.cn (Tianhe Xu), wjtsci2015@163.com (Junting Wang), zhanghao@ouc.edu.cn (Hao Zhang)

*URL:* www.weiwilliamhuang.cn (Wei Huang)

tal results on real open dataset show that the proposed model outperforms other state-of-the-art methods, which achieves an accuracy with an error of less than 0.3m/s. Specifically, MDF-RAGAN not only outperforms convolutional neural network (CNN) and spatial interpolation (SITP) by nearly a factor of two, but also achieves about 65.8% root mean square error (RMSE) reduction compared to mean profile, which fully reflects the enhancement of overall profile matching by multi-source fusion and cross-modal attention.

*Keywords:* Sound speed profile (SSP), Sound speed field construction, Generative adversarial network (GAN), Data fusion

---

## 1. Introduction

The estimation of underwater sound velocity distribution has become a research hotspot in recent years, as it affects the propagation mode of underwater signals and therefore has a critical impact on the energy efficiency of underwater acoustic communication and accuracy of underwater acoustic positioning (Erol-Kantarci et al., 2011; Piccolo et al., 2019; Luo et al., 2021).

Traditionally, sound speed profiles (SSPs), that are popular adopted to describe the distribution of sound speed, are usually measured by conductivity, temperature, and depth profiler (CTD) or sound velocity profiler (SVP) (Wang et al., 2014), but these instruments rely on shipborne deployment systems, leading to expensive economic and labor costs. To improve the efficiency of measuring sound velocity distribution, scholars have proposed several methods for inverting sound velocity distribution leveraging sonar observation data, based on the influence of sound velocity distribution on the sound field. These methods can be mainly divided into 3 categories: matching field processing (MFP) (Tolstoy et al., 1991; Li and Zhang, 2010; Zhang et al., 2012, 2015), compressive sensing (CS) (Bianco and Gerstoft, 2017; Choo and Seong, 2018), and deep learning (DL) (Stephan et al., 1995; Huang et al., 2021b, 2023).

MFP is a method of determining the sound velocity distribution by simulating the SSP and its corresponding theoretical sound field distribution, and matching it with the measured sound field based on ray theory or normal wave theory. In order to improve the computational efficiency of MFP, heuristic algorithms, such as particle swarm optimization (PSO) (Tolstoy et al., 1991) and genetic algorithm (GA) (Zhang et al., 2015), are usually introduced for accelerating the search process of feature vector coefficients.

However, heuristic algorithms still have very high computational complexity and the results obtained are prone to getting stuck in local optima, which affects the accuracy of sound velocity inversion.

Considering that ray theory or normal wave theory can only establish a mapping relationship from sound velocity distribution to sound field distribution, scholars have begun to explore how to directly establish a mapping relationship from sound field distribution to sound velocity distribution. The CS technology achieves this process through a feature mapping dictionary, which further improves the efficiency of sound speed estimation compared to MFP. However, the dictionary establishment process introduces linearization approximation (Bianco and Gerstoft, 2017), which sacrifices the accuracy of sound speed construction.

During the last decades, DL has obtained significant achievement in the field of data processing, benefiting from its ability to handle complex nonlinear mapping relationships. The DL based sound velocity inversion method not only reduces accuracy loss, but also maintains the real-time advantage at the working stage (training can be completed in advance) (Huang et al., 2021b, 2023). However, above mentioned SSP inversion methods highly rely on sonar observation data, which put forward strict requirements on the deployment of sonar observation systems, making it difficult to achieve large-scale ocean coverage.

Recently, to eliminate the need for underwater on-site data measurement, scholars have proposed two ways of approaches to improve the efficiency of sound velocity estimation: one is using historical sound velocity data to forecast the current sound velocity from the perspective of time series prediction, and the other is fusing the remote sensing sea surface temperature (SST) data and historical sound velocity data to estimate the sound velocity distribution from the perspective of spatial sound velocity field construction. In 2023, Piao et al. proposed an SSP prediction method under internal waves based on long short-term memory (LSTM) neural networks (Piao et al., 2023). Lu et al. further developed a hierarchical LSTM (H-LSTM) model that predict sound speed distribution at different depth layers (Lu et al., Jan., 2024). However, the sound velocity prediction method is only applicable to areas with sufficient historical sound velocity distribution, which can not be satisfied in some ocean areas due to difficulty in measuring SSPs.

To tackle this issue, Li et al. (Li et al., Aug., 2021) and Wu et al. (Wu et al., 2024) both proposed SSP construction methods fusing SST data and historical SSPs, where a self-organized mapping (SOM) neural network

was proposed in (Li et al., Aug., 2021) and a convolutional neural network (CNN) was proposed in (Wu et al., 2024). However, both (Li et al., Aug., 2021) and (Wu et al., 2024) focus excessively on local spatial correlations while neglecting global spatial relationships, resulting in substantial accuracy limitations.

To achieve high-precision estimation of sound velocity distribution in a given sea area without on-site underwater data measurement, we propose a multi-modal data-fusion generative adversarial network model with residual attention block (MDF-RAGAN) for SSP construction. We aim to improve the model’s ability for capturing global spatial feature correlations by the attention mechanisms, and use residual modules for deeply capturing small disturbances in the deep ocean sound velocity distribution caused by changes of SST. The contributions of this work are summarized as follows.

- To quickly obtain sound velocity distribution of a given area, we proposed a MDF-RAGAN model that fusing SST data with historical sound velocity distribution, which eliminates the need for underwater on-site data measurement. The generator is used to establish a mapping relationship from the fused data to the sound velocity distribution, while the discriminator is used to constrain the trend of the sound velocity distribution.
- To improve the accuracy of underwater sound velocity construction, we integrated the residual attention block into the multi-modal data-fusion GAN model. With the residual block, the model could learn the influence of SST on the variation of sound velocity. With the attention mechanism, the model could learn the correlation of sound velocity distribution in large-scale spatial regions.
- To evaluate the feasibility of the proposed MDF-RAGAN model, the performance was tested on real sampled SSP and SST data. Results show that MDF-RAGAN surpasses the state-of-the-art (SOTA) models in the field of sound velocity distribution estimation.

The rest part of this paper is organized as follows. Section 2 describes the MDF-RAGAN in detail. Section 3 evaluates and discusses the performance of MDF-RAGAN on real-word open dataset. The conclusion is given in Section 4.

## 2. Sound Speed Field Construction by MDF-RAGAN

### 2.1. Overview of MDF-RAGAN Framework

In this paper, we aim to construct the SSP of a target location with the help of SST data and SSP distribution of neighboring locations. This task is significantly challenging: firstly, the spatial coordinates, SST and SSPs are heterogeneous modal data, which need to be efficiently aligned and fused in a unified feature space; secondly, the SSPs show highly nonlinear variations with environmental variables such as depth, temperature, salinity, etc., which puts stringent requirements on the network’s expressive ability.

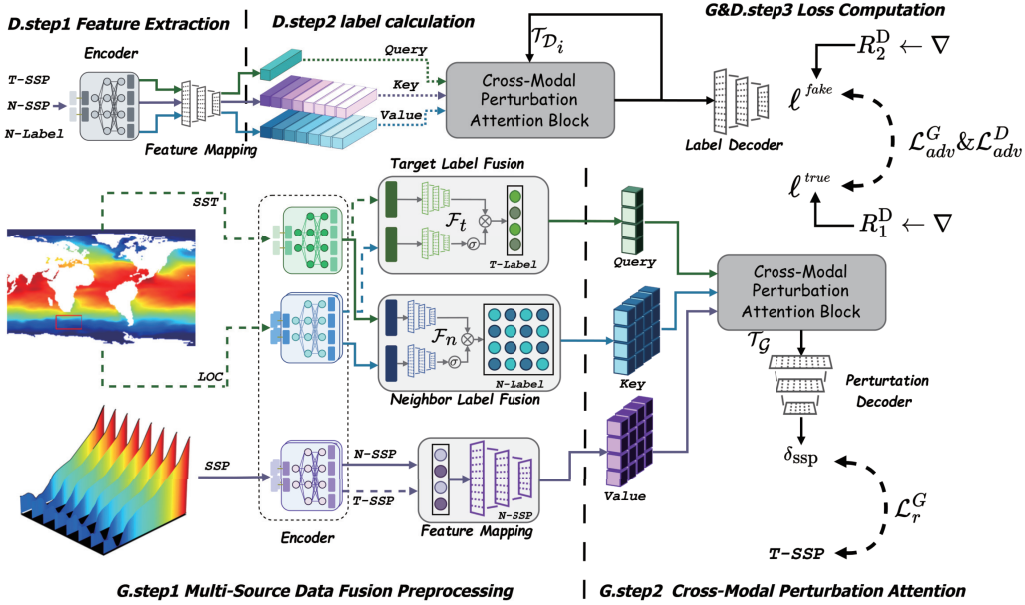


Figure 1: Framework of SSP estimation based on the MDF-RAGAN

To address these challenges, we propose the MDF-RAGAN, a novel framework consisting of three key components as shown in Fig. 1. We first map three types of heterogeneous data modalities, namely, geographic coordinates of the target point and its surrounding grid, SST, and historical SSPs, into a unified feature space by multi-source data fusion preprocessing; subsequently, we use the cross-modal perturbation attention block to capture the spatial correlation between sound velocity distributions; finally, the end-to-end optimization strategy is constructed by combining the generative adversarial

training and the multi-task regression loss to ensure a high level of prediction performance under a small number of samples.

The input of the model are coordinates, SST and historical SSPs. Let the set of SSPs at the reference points surrounding a given latitude-longitude coordinate be denoted as  $\mathbf{R}_{ssp}^n \in \mathbb{R}^{N \times D}$ , where  $N$  denotes the number of surrounding reference points, and  $D$  represents the depth dimension. The geographic coordinates (longitude  $\lambda$ , latitude  $\phi$ ) and the SST obtained by remote sensing at each reference point are denoted by  $\mathbf{R}_{loc}^n \in \mathbb{R}^{N \times 2}$ ,  $\mathbf{R}_{sst}^n \in \mathbb{R}^{N \times 1}$ . The geographic coordinates and the sea surface temperature at the target point are denoted as  $\mathbf{R}_{loc}^t \in \mathbb{R}^{1 \times 2}$ ,  $\mathbf{R}_{sst}^t \in \mathbb{R}^{1 \times 1}$ .

The final output from the generator network is a small perturbation  $\delta_{ssp}$  at the target location. Therefore, the estimated SSP  $\hat{\mathbf{s}}_{ssp}$  at the target point can be expressed as the sum of the mean SSP of surrounding reference points and the generated perturbation:

$$\hat{\mathbf{s}}_{ssp} = \frac{1}{N} \sum_{n=1}^N \mathbf{R}_{ssp}^n + \delta_{ssp} \quad (1)$$

This decomposition approach guides the generator network to focus explicitly on the local variability at the target point. Leveraging the overall trend information from surrounding reference points, we represent the estimated SSP as the sum of a mean profile of surrounding references and a small perturbation term. The perturbation term is learned by the generator network to compensate for inadequacies inherent in the mean profile model, especially under complex marine conditions, thereby effectively enhancing prediction accuracy. Moreover, such decomposition simplifies model training, enabling the network to focus more effectively on capturing deep nonlinear deviations rather than merely reconstructing the background mean.

The detailed model of MDF-RAGAN is given in Fig. 2. In the following section, we will introduce the generator, discriminator, and optimization strategy step by step.

## 2.2. Generator

The core objective of the generator is to map the fused features from multiple sources to detailed perturbations of the SSP at the target location, and thus reconstruct temperature-induced variations in the ocean on the sound velocity distribution. The entire network consists of three stages in sequence:

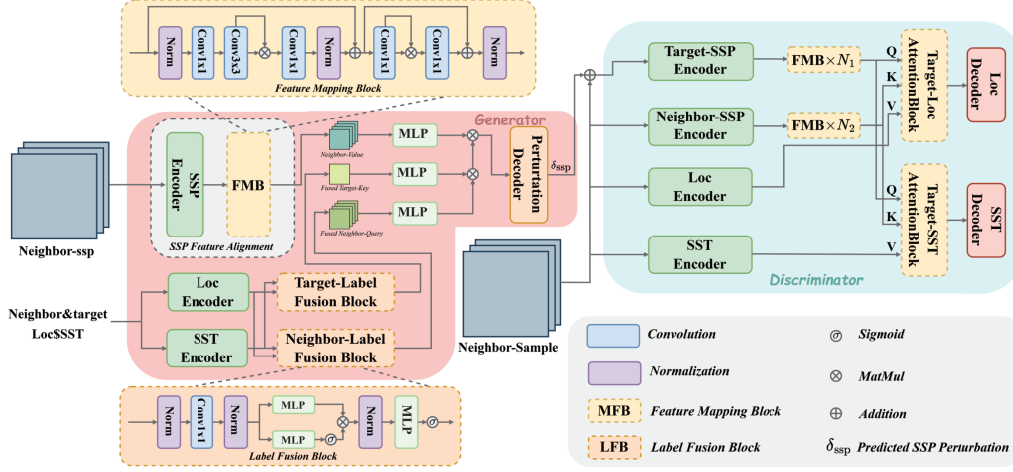


Figure 2: The proposed MDF-RAGAN model for SSP estimation, which consists of a generator and a discriminator, incorporating FMB, LFB, and CMPAB for effective multi-source data fusion.

feature encoding and fusion, cross-modal cross-attention, and perturbation decoding.

### 2.2.1. Multi-Source Data Fusion Preprocessing

The SSP shows complex nonlinear behaviors with the variations in ocean depth, temperature and salinity. The geographic coordinates identify the thermohaline structure of the ocean region, while the SST distribution directly affects the surface thermohaline gradient, which in turn has a significant effect on the upper sound speed distribution. To accurately estimate the SSP at target points, it is necessary to effectively align and fuse multi-sources of data, including geographic coordinates and SST, within a unified feature space to make full use of their physical complementarities.

*Label Fusion Block.* The label fusion block (LFB) aims to adaptively fuse the label information from both the target point and surrounding reference points. Specifically, the latitude and longitude coordinates and SST obtained by remote sensing are first embedded into the feature space  $d_r$  through their corresponding encodings, each undergoing linear mapping followed by layer normalization:

$$\mathbf{z}_{loc}^t = W_{loc} \mathbf{R}_{loc}^t + b_{loc}, \quad (2)$$



$$\mathbf{z}_{sst}^t = W_{sst} \mathbf{R}_{sst}^t + b_{sst}, \quad (3)$$

where  $W_{loc} \in \mathbb{R}^{2 \times d_r}$  and  $W_{sst} \in \mathbb{R}^{1 \times d_r}$  are the linear transformation matrices that map these two types of inputs to the  $d_r$ -dimensional feature space, with the corresponding bias terms being  $b_{loc} \in \mathbb{R}^{d_r}$  and  $b_{sst} \in \mathbb{R}^{d_r}$ . Thus, we can obtain the  $d_r$ -dimensional embedding feature vectors for surface remote sensing temperature and coordinate points.

The same feature transformations are applied to the corresponding reference point data, mapping the reference point features  $\{\mathbf{z}_{sst}^{r,n}, \mathbf{z}_{loc}^{r,n}\}_n^N$  into a consistent dimension. The aligned labels are concatenated along the sample dimension to form the fusion matrix  $\mathbf{Z}^r \in \mathbb{R}^{N \times d_r}$ . Subsequently, the LFB is employed to fuse the features across both the sample and feature dimensions. An initial fusion is performed via a learnable convolutional transformation:

$$\tilde{\mathbf{Z}}^r = \gamma_1 \frac{\mathbf{Z}^r - \mu_Z}{\sigma_Z} + \beta_1, \quad (4)$$

$$\bar{\mathbf{Z}}^r = \gamma_2 \frac{\mathbf{W} \times \tilde{\mathbf{Z}}^r + \mathbf{b} - \mu_Y}{\sigma_Y} + \beta_2, \quad (5)$$

where  $\mu_Z, \sigma_Z$  are the mean and standard deviation computed along the channel dimension of the matrix  $\mathbf{Z}^r$ ,  $\mu_Y, \sigma_Y$  denote the corresponding statistics computed after the convolution operation, and  $\gamma_1, \beta_1$  and  $\gamma_2, \beta_2$  are the learnable scaling and shifting parameters normalized twice. After the transformation, we divide the fusion matrix  $\bar{\mathbf{Z}}^r$  into two parts  $\bar{\mathbf{Z}}_A^r, \bar{\mathbf{Z}}_B^r \in \mathbb{R}^{N \times d_r}$  and feed them to the linear gating unit GLU:

$$\mathbf{Z}_L = \bar{\mathbf{Z}}_A^r \odot \sigma(\bar{\mathbf{Z}}_B^r). \quad (6)$$

This enables adaptive weighting across labels from different modalities. The proposed mechanism dynamically adjusts the relative importance of coordinates and temperature in SSP predictions according to the geographic and thermal conditions of various ocean regions.

*Feature Mapping Block.* Considering that the detailed variations of SSP along the depth dimension are closely associated with the locations of scattering layers and thermoclines, the Feature Mapping Block (FMB) further enhances these physical characteristics through local context modeling. Given the SSP features at the reference points  $\mathbf{Z}_{ssp}^r \in \mathbb{R}^{1 \times N \times d_r}$ , the FMB initially extracts fine-grained, depth-wise features through depthwise separable convolutions:

$$\dot{\mathbf{Z}}_{ssp}^r = \text{DSCConv}(\mathbf{Z}_{ssp}^r). \quad (7)$$

Specifically, the calculation can be expressed as follows:

$$Y_{i,j} = \sum_{u=1}^{k_h} \sum_{v=1}^{k_w} K_{u,v}^{(dw)} \left( \dot{\mathbf{Z}}_{ssp}^r \right)_{i+u-1, j+v-1}, \quad (8)$$

$$\left( \dot{\mathbf{Z}}_{ssp}^r \right)_{i,j} = K_d^{(pw)} Y_{i,j} + b_d, \quad (9)$$

where  $K^{(dw)} \in \mathbb{R}^{1 \times k_h \times k_w}$  is the depthwise convolution kernel, which performs  $k_h \times k_w$  convolutions independently on each channel.  $K^{(pw)} \in \mathbb{R}^{1 \times 1 \times 1 \times 1}$  and  $b \in \mathbb{R}^1$  denote the kernel and bias used in the subsequent pointwise convolution. In deep-sea environments, abrupt variations in salinity across adjacent depth levels may amplify gradients during training. To mitigate potential gradient explosion introduced by convolutional operations alone, we further apply a SimpleGate activation module after convolution:

$$SG\left(\dot{\mathbf{Z}}_{ssp}^r\right) = \dot{\mathbf{Z}}_{ssp}^r \odot \dot{\mathbf{Z}}_{ssp}^r. \quad (10)$$

These variations are captured and in turn enhanced features are constructed using residual linking and scaling factors:

$$\mathbf{Z}_{fmb}^{r,n} = \mathbf{Z}_{ssp}^r + \xi \cdot SG\left(\dot{\mathbf{Z}}_{ssp}^r\right), \quad (11)$$

where the weight  $\xi$  is a learnable scaling factor used to balance the relative contributions of the original depth features  $\mathbf{Z}_{ssp}^r$  and the enhanced features  $SG\left(\dot{\mathbf{Z}}_{ssp}^r\right)$  in the residual link. Through training, the model automatically adjusts the size of  $\xi$ : when  $\xi$  is large, it emphasises the local nonlinear changes captured by the depthwise separable convolution and SimpleGate; when  $\xi$  is small or even close to 0, it focuses more on preserving the overall trend of the SSP.

This design not only improves the sensitivity of the model to transition zones such as the thermocline and scattering layer, but also effectively emphasises local deviations while preserving the overall trend, which helps the generator to accurately simulate the detailed variations in the SSP at the target point.

Through synergistic interaction between the LFB and FMB, the module achieves the unified alignment and enhancement of multimodal labeling information with deep spatial context features. This integration provides MDF-RAGAN with rich, structured, and physically meaningful initial features, thereby supporting robust and precise adversarial learning.

### 2.2.2. Cross-Modal Perturbation Attention Block

After feature encoding and fusion, we obtain the SSP features from the reference point and the fused label embeddings of the target and reference points after processing by the label fusion module  $\mathbf{Z}_L^t \in \mathbb{R}^{1 \times d_r}$ ,  $\mathbf{Z}_L^{r,n} \in \mathbb{R}^{N \times d_r}$ . The goal is to accurately predict the fine-grained perturbation of the SSP at the target point based on the label information. To this end, we propose the Cross-Modal Perturbation Attention Block module to capture the cross-modal dependencies and guide the perturbation modeling process.

Specifically, we treat the fused label embedding of the target point as the query  $\mathbf{Q}$ , the fused label embeddings of the reference points as the key  $\mathbf{K}$ , and the reference SSP features of the surrounding points as the value  $\mathbf{V}$ . These tensors are then passed through learned linear projections to obtain the initial query, key, and value matrices:

$$Q^{(0)} = \mathbf{Z}_L^t W_Q^{(0)} + b_Q^{(0)}, K^{(0)} = \mathbf{Z}_L^{r,n} W_K^{(0)} + b_K^{(0)}, V^{(0)} = \mathbf{Z}_{fmb}^{r,n} W_V^{(0)} + b_V^{(0)}. \quad (12)$$

To ensure that longitudinal depth-wise positional information is not lost during the computation of attention, an aligned positional encoding is required. That is, a learnable positional encoding  $PE \in \mathbb{R}^{D \times d}$  is superimposed to each vector, allowing the model to correctly distinguish the natural order of sound speed profiles at different depths. The cross-modal attention mechanism requires a number of computations, of which the  $l$ -th layer of computation can be expressed as:

$$X^{(l)} = \frac{Q^{(l-1)} (K^{(l-1)})^T}{\sqrt{d}}, m_i^{(l)} = \max_j X_{ij}^{(l)}, \quad (13)$$

$$A_{ij}^{(l)} = \frac{\exp(X_{ij}^{(l)} - m_i^{(l)})}{\sum_{j'} \exp(X_{ij'}^{(l)} - m_i^{(l)})}, O^{(l)} = A^{(l)} V^{(l-1)}. \quad (14)$$

In the above calculation,  $d$  denotes the dimension size of the query and key vectors, and  $l$  denotes the index of the attention layer. The elements

of the unnormalised score matrix  $X^{(l)} \in \mathbb{R}^{N \times N}$  represent the similarity between the  $i$ -th query and the  $j$ -th key.  $m_i^{(l)} = \max_j X_{ij}^{(l)}$  takes the maximum value of each row to stabilise the values before the Softmax operation. The normalised attention weights  $A_{ij}^{(l)}$  represent the model’s attention intensity for each key, and the final output matrix  $O^{(l)}$  is the weighted sum whose dimensions are consistent with  $V^{(l-1)}$ . The subscripts  $i$  and  $j$  correspond to the query position and key/value position in the sequence (or depth layer), respectively.

Considering that multiple calculations may produce exploding gradients, here we subtract the maximum value of each row when calculating Softmax, which can effectively avoid the exploding-gradient problem during training caused by too large or too small values. Temperature, salinity, and pressure often vary in magnitude from one reference point to another, and with this adaptive logit normalization, the model is able to propagate multi-point information into each depth level with more balanced weights, thus simulating a weighted contribution effect similar to that of interpolation.

The attention output  $O^l$  is processed with FFN activation function and layer normalization to increase non-linear representational capacity:

$$H^{(l)} = W_2^{(l)} \text{GELU}(W_1^{(l)} \text{LN}(O^{(l)} + b_1^{(l)}) + b_2^{(l)}). \quad (15)$$

The residual connection adds  $O^l$  to the layer input, stabilizing deep-layer information propagation and maintaining smooth gradient flow. After the  $l$ -th cross-modal attention layer, the resulting feature  $H^l$  is fed into a perturbation decoding head to predict the fine-grained SSP perturbation through a two-layer fully connected network:

$$\delta_{ssp} = W_{dec2} \text{GELU}(W_{dec1} H^{(L)} + b_{dec1}) + b_{dec2}. \quad (16)$$

This perturbation is added to the mean SSP of the reference points to generate the final prediction  $\hat{\mathbf{s}}_{ssp}$ . In summary, the cross-modal attention mechanism in the generator combined with the numerical stabilization strategy mimics the balanced distribution of the contributions from each detection point in the acoustic-profile interpolation, and exploits the nonlinear capability of the deep network to capture the complex sound velocity structures such as thermocline and scattering layer, thus achieving a fine-grained prediction of the SSP perturbation at the target point.

### 2.3. Discriminator

The core of the discriminator is to distinguish between real and generated SSP samples, and to provide more informative gradient signals to the generator through multi-task regression. The discriminator accepts two types of target SSP inputs: the real samples  $\mathbf{s}_{ssp}^{real} \in \mathbb{R}^D$  and the generated samples  $\mathbf{s}_{ssp}^{fake} = \frac{1}{N} \sum_{i=1}^N \mathbf{R}_{ssp,i}^n + \delta_{ssp} \in \mathbb{R}^D$  output by the generator, which, together with the real reference point samples, constitute the inputs to the discriminator network:

$$X_{in} = [\mathbf{s}_{ssp}; \mathbf{R}_{ssp}^n; \mathbf{R}_{sst}^n; \mathbf{R}_{loc}^n] \quad (17)$$

Similarly, we encode the input target SSP  $\mathbf{s}_{ssp}$  of unknown authenticity and the real reference point SSP  $\mathbf{R}_{ssp}^n$  respectively, and also encode the coordinate information  $\mathbf{R}_{loc}^n$  and SST obtained by remote sensing  $\mathbf{R}_{sst}^n$  of the reference point, aligned to the same feature space. After the correct SSP is extracted by FMB, the sequence of SSPs and the labeling information jointly participate in feature learning collaboratively.

Here we use the coordinates of the target point and the SST as the output of the discriminator, which is used as an alternative to the traditional way of training the discriminator in terms of realism. The input tensor is stacked with the same multi-layer stack of cross-modal attention blocks and position-wise feed-forward networks used in the generator, where the Query is the SSP feature vector of the target point  $\mathbf{Z}_{ssp}^t$ , the Key is the SSP feature vector of the reference point  $\mathbf{Z}_{ssp}^{r,n}$ , and the Value corresponds to the feature vector encoded by the coordinates of the reference point, and the feature vector encoded by the SST  $\mathbf{Z}_{loc}^{r,n}$  and  $\mathbf{Z}_{sst}^{r,n}$ , respectively. The formula for each layer of attention is similar to the computational strategy of the generator:

$$O^{(l)} = \text{Soft max} \left( \frac{Q^{(l-1)} K^{(l-1)\text{T}} - m^{(l)}}{\sqrt{d}} \right) V^{(l-1)}, \quad (18)$$

$$m^{(l)} = \max_j \left( \frac{Q^{(l-1)} K_{:,j}^{(l-1)\text{T}}}{\sqrt{d}} \right). \quad (19)$$

This numerical-stabilization trick subtracts the row-wise maximum logit before the soft-max, mitigating exploding or vanishing gradients and reducing the risk of mode collapse during adversarial training.

After obtaining the output features  $H_{loc}^{(l)} \in \mathbb{R}^{1 \times d_r}$  and  $H_{ssp}^{(l)} \in \mathbb{R}^{1 \times d_r}$ , we split into two branches, where the coordinate regression branch maps the

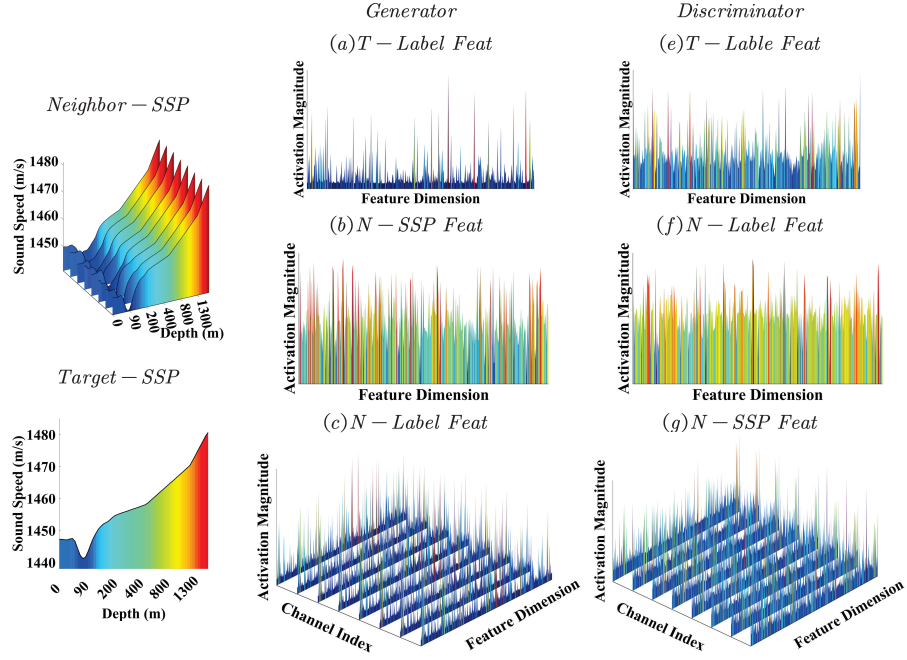


Figure 3: Visualization of intermediate features in the MDF-RAGAN model. (a)-(c) represent the intermediate outputs from the generator, while (d)-(f) show the intermediate feature outputs from the discriminator. Specifically: (a) represents the fused label features of the target point, (b) represents the SSP features of surrounding sample points, (c) represents the fused label features of surrounding sample points, (d) represents the fused label features of the target point, (e) represents the fused label features of surrounding sample points, and (f) represents the SSP features of surrounding sample points.

latitude and longitude of the target point, and the SST regression branch predicts the sensing SST through a similar fully connected layer:

$$\hat{\mathbf{t}}_{loc} = W_{loc}H_{loc}^{(l)} + b_{loc}, \quad (20)$$

$$\hat{\mathbf{t}}_{sst} = W_{sst}H_{sst}^{(l)} + b_{sst}, \quad (21)$$

The above multi-task outputs, without adding extra parameters, enable the discriminator to both improve its sensitivity to differences in SSP details and provide the generator with error signals for both coordinates and SST, promoting stable convergence and improving the accuracy of the overall network in complex underwater acoustic environments. Fig. 3 visualizes the fused feature of generator and discriminator.

#### 2.4. Optimization Strategy

In this section, the loss function as well as different training strategies are designed mainly for the generator and the discriminator, so as to balance the stability of the game-based training as well as the accuracy of the SSP perturbation reconstruction. The generator loss mainly consists of the relativistic Softplus GAN loss and the centroid SSP reconstruction loss. Specifically, the discriminator produces two sequences of realism scores for real target-point SSP samples:

$$\ell_i^{real} = D(\mathbf{s}_{ssp}^{real}; \mathbf{R}_{ssp}^n; \mathbf{R}_{sst}^n; \mathbf{R}_{loc}^n), \quad (22)$$

$$\ell_i^{fake} = D(\mathbf{s}_{ssp}^{fake}; \mathbf{R}_{ssp}^n; \mathbf{R}_{sst}^n; \mathbf{R}_{loc}^n). \quad (23)$$

Then the generator against loss is defined as:

$$\mathcal{L}_{adv}^G = -\frac{1}{B} \sum_{i=1}^B \text{Softplus}(\ell_i^{fake} - \ell_i^{real}). \quad (24)$$

The minus sign is to allow the generator to approximate the true SSP distribution by maximizing the fake-sample score, thus ensuring that the SSP data at the target point can be correctly reconstructed from the label data. The generator also introduces an root mean square error (RMSE) loss of the SSP at the center-point in order to approximate the true value:

$$\mathcal{L}_r^G = \frac{1}{B} \sum_{i=1}^B \sqrt{\frac{1}{D} \sum_{j=1}^D (s_{ij}^{real} - s_{ij}^{fake})^2}, \quad (25)$$

where  $s_{ij}^{real}$  and  $s_{ij}^{fake}$  denote the true and predicted values of the  $i$ -th sample at depth  $j$ , respectively,  $B$  is the batch size, and  $D$  is the number of depth points. Combining the two losses, the total loss of the generator can be expressed as:

$$\mathcal{L}_G = \mathcal{L}_{adv}^G + \eta \mathcal{L}_r^G \quad (26)$$

The loss function of the discriminator consists of an adversarial true-false branch as well as a zero-centered gradient penalty. The adversarial branching uses the relative discriminative power of the generated versus true samples along the Softplus form of the metric:

$$\mathcal{L}_{adv}^D = \frac{1}{B} \sum_{i=1}^B \text{Softplus}(\ell_i^{fake} - \ell_i^{real}). \quad (27)$$

A zero-centered gradient penalty is also introduced in order to limit training instability due to too large a gradient, and the R1 and R2 terms are computed separately for real and generated samples:

$$R_1^D = \mathbb{E}_{\mathbf{s}^{real}} [|\nabla_{\mathbf{s}} D(\mathbf{s}^{real}, \mathbf{R}_{ssp}^t)|_2^2], \quad (28)$$

$$R_2^D = \mathbb{E}_{\mathbf{s}^{fake}} [|\nabla_{\mathbf{s}} D(\mathbf{s}^{fake}, \mathbf{R}_{ssp}^t)|_2^2]. \quad (29)$$

In Eqs. (28) and (29), the zero-centred gradient penalty terms  $R_1^D$  and  $R_2^D$  measure the gradient magnitude of the discriminator on the real sample distribution  $\mathbf{s}^{real}$  and the generated sample distribution  $\mathbf{s}^{fake}$ , respectively. Specifically,  $\mathbb{E}_{\mathbf{s}^{real}}$  and  $\mathbb{E}_{\mathbf{s}^{fake}}$  denote the expectation over the distributions corresponding to the real and fake samples; and  $\nabla_{\mathbf{s}} D(\mathbf{s}, \mathbf{R}_{ssp}^t)$  is the gradient of the discriminator's output  $D$  with respect to its input sound speed profile  $\mathbf{s}$ , where the conditional input  $\mathbf{R}_{ssp}^t$  represents the reference sound speed profiles.

Eventually we can get the total loss function representation of the discriminator:

$$\mathcal{L}_D = \mathcal{L}_{adv}^D + \eta_1 R_1^D + \eta_2 R_2^D. \quad (30)$$



In order to guarantee the stability and convergence effect of MDF-RAGAN in the early stage of adversarial training, we adopt a staged training strategy, in the first stage, we only optimise the generator parameters  $\theta_G$ , the discriminator parameters keep  $\theta_D$  kept frozen and not updated, at this time through the

$$\theta_G \leftarrow \theta_G - \eta_t \nabla_{\theta_G} \mathcal{L}_G. \quad (31)$$

In the first stage, the generator learns an initial mapping from the multi-source fused label embeddings to the SSP perturbations at the target point. A linear learning-rate warm-up is applied, and the network parameters are updated solely with the generator loss  $\mathcal{L}_G$ . In the second stage, training switches to adversarial learning: network parameters are alternately updated with the generator loss  $\mathcal{L}_G$  and the discriminator loss  $\mathcal{L}_D$ , enabling joint optimization of both networks.

The learning rate  $\eta_t$  can be scheduled using the cosine annealing learning rate:

$$\eta_t = \eta_{\min} + \frac{1}{2} (\eta_{\max} - \eta_{\min}) \left( 1 + \cos\left(\pi \frac{t}{T}\right) \right) \quad (32)$$

where  $T$  is the total number of epochs and  $t$  is the current epoch,  $\eta_{\max}$  is the maximum initial learning rate used at the end of warm-up and  $\eta_{\min}$  is the minimum learning rate at the end of annealing. Such a staged training strategy effectively ensures that the generator obtains a robust initial mapping without the disturbance first, and obtains a more accurate prediction of the sound speed perturbation in the subsequent adversarial phase by alternating game-like training.

### 3. Results and Discussions

#### 3.1. Experimental Setting

##### 3.1.1. Dataset

In this study, an experimental dataset was constructed on the sea area (gridded  $1^\circ \times 1^\circ$  latitude and longitude) from  $59.5^\circ$  to  $39.5^\circ$  S and  $0.5^\circ$  to  $38.5^\circ$  E, combining Argo observations and remotely sensed information.

SSP data were taken from the GDCSM Argo gridded Argo dataset (Li Hong, 2017), and the raw observation profiles covered 0-1976 m depth with 58 scattered points, which were linearly interpolated depth-by-depth to 1 m intervals to generate 1977-dimensional high-resolution SSP vectors. SST data were obtained from the NOAA OISST monthly average product (Huang et al.,

2021a), spatially mapped and aligned to an Argo grid to obtain the current month’s SST values for each grid point.

In order to make full use of the spatial neighborhood information, each  $1^\circ \times 1^\circ$  grid is taken as the center point, and a  $3 \times 3$  sliding window is formed with its surrounding eight adjacent grid points. The interpolated SSP at the center is used as the estimation target, and the coordinates, SST and SSP of the remaining eight grid points are processed by the LFB with the FMB to output the multimodal input features used for generator perturbation estimation.

In terms of timing, to assess the impact of different historical data lengths on model performance, the training set is divided into three time windows: January 2004-December 2020, January 2011-December 2020, and January 2016-December 2020; the test set uniformly January 2021-June 2023 data were used. During spatial sampling, the training samples are extracted at  $3^\circ$  intervals along the latitude and longitude directions to ensure that there is no data leakage during testing; the test samples are offset by  $3^\circ$  on the basis of the training grid to achieve spatial non-overlapping coverage, ensuring that the training and testing areas are spatially complementary and without overlap.

Leveraging the above multi-source fusion and sliding-window sampling strategy, we construct a high-quality dataset containing thousands of spatiotemporally matched samples. This dataset provides a solid foundation for validating the model’s generalization ability under different historical windows, unseen spatial regions, and multimodal feature settings.

### 3.1.2. Performance Evaluation Metrics

To evaluate the accuracy and robustness of the model for estimating SSPs at target points, the RMSE was adopted in this paper. Let the test set contain  $N_{te}$  samples, the true SSP at the target point for the first  $n$  sample is noted as  $\mathbf{s}_n^t$  and the generator predicts the profile as  $\hat{\mathbf{s}}_n^t$ , then the RMSE denotes the average of  $L_2$  distance:

$$\text{RMSE} = \sqrt{\frac{1}{N_{te}} \sum_{i=1}^{N_{te}} \|\hat{\mathbf{s}}_n^t - \mathbf{s}_n^t\|_2} \quad (33)$$

This indicator visualizes the magnitude of the absolute error between the generated profile and the true observation.

### 3.1.3. Parameter Initialization

All experiments were conducted on a Linux server equipped with a single NVIDIA RTX 3090 (24 GB) and an Intel Xeon Gold 6330 CPU. Training and inference were implemented in PyTorch.

The generator and discriminator share an embedding dimension (hidden size) of 384, with a dropout rate and attention-dropout rate of 0.05. Each network uses [2, 2] Transformer blocks connected via residual paths.

Training hyper-parameters were set as follows: batch size 128, epochs 196, learning rate of the generator  $lr_g = 4 \times 10^{-4}$ , learning rate of the discriminator  $lr_d = 5 \times 10^{-4}$ . The learning rate was linearly warmed up for the first 20 epochs and then decayed with cosine annealing, then the minimum learning rate was  $lr_{min} = 1 \times 10^{-7}$ , and the weight decay was set to be  $1 \times 10^{-3}$ . Data loading employs 8 data-loader workers.

## 3.2. Baselines

In order to comprehensively validate the performance enhancement of the proposed MDF-RAGAN model in SSP estimation, three types of baseline methods are selected in this study: averaged profile based on historical statistics, spatial interpolation (SITP), and convolutional neural network (CNN) (Wu et al., 2024). Quantitative results show that MDF-RAGAN, by effectively fusing physical priors and modelling nonlinear interactions, consistently outperforms these baselines.

### 3.2.1. Mean Profile

In the simplest historical statistical baseline, we compute the mean value of the sound velocity for each depth layer in the training set and use that average profile as an estimation for the corresponding depth for all test points. Let there be a total of  $N$  sample points around the target point, the mean profile estimation equation is:

$$\hat{s}^{avr} = \frac{1}{N} \sum_{i=1}^N s_i^{ngb} \quad (34)$$

### 3.2.2. Spatial Interpolation

We mainly use the inverse distance weighting method to assign different weights to the estimated values for each depth layer by considering the spatial distance between the target point and its surrounding consistent sample

points. Specifically, for the location  $(x, y)$ , the interpolated SSP is:

$$\hat{\mathbf{s}}^{IDW}(x, y) = \frac{\sum_{n=1}^N \varpi_n \mathbf{s}_n}{\sum_{n=1}^N \varpi_n}, \varpi_n = \frac{1}{D_n^p} \quad (35)$$

where  $D_n = \sqrt{(x - x_n)^2 + (y - y_n)^2}$ , is the in-plane distance between the target point and the location of the first  $n$  known profile, usually taken as a power exponent  $p = 2$ . The SITP method weights historical observations within a geographic neighborhood, and can capture the effects of thermohaline gradients at spatially adjacent points to some extent.

### 3.2.3. CNN Model

As a deep learning baseline, this study implements a classical CNN model for comparing the performance of deep networks in SSP tasks (Wu et al., 2024). The model takes the center and eight profile vectors, corresponding coordinates and SST of its  $3 \times 3$  neighborhood grid as multi-channel inputs, and extracts local features in the depth dimension through three-layer one-dimensional convolution (convolution kernel width of 3, channel numbers of 64, 128 and 256 in turn), ReLU activation and maximum pooling; subsequently, the perturbation value of the center is outputted by the regression of the two-layer fully-connected network. During the training process, the CNN is also optimized using the RMSE as the loss function.

## 3.3. Accuracy Performance

### 3.3.1. Influence of Training Data Length

To evaluate the influence of training data length on model accuracy performance, Fig. 4 compares the estimation performance of models trained using three historical windows of 5 years (2016-2020), 10 years (2011-2020) and 17 years (2004-2020) on the same sea profile. As shown in the figure, the window length from 3 to 10 years extends the RMSE of each method in a decreasing trend, but the MDF-RAGAN can achieve an RMSE of about 0.18 m/s under the condition of the shortest 3 years of data, and with the increase of the training years its error further converges to about 0.14 m/s, without any significant decrease, which indicates that the model already has a strong representation ability for a small number of historical samples.

In addition, Table 1 compares the RMSE of MDF-RAGAN trained on 5, 10 and 17 years of historical data with the corresponding CNN, as well as SITP with the historical mean (MEAN) method, at four different depths (200

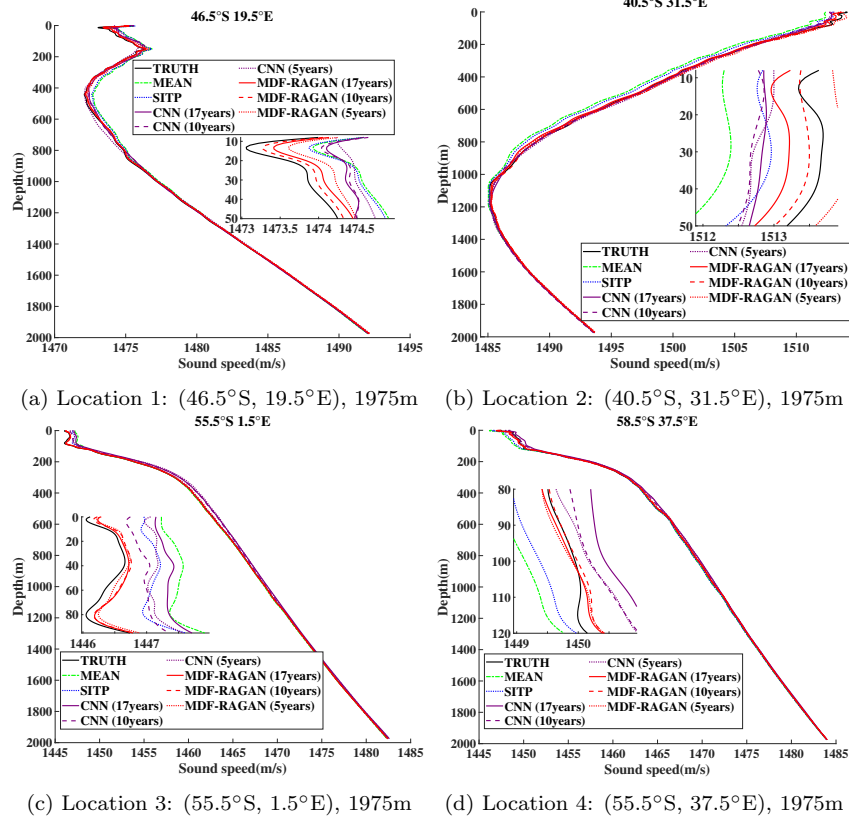


Figure 4: Comparison of sound speed profile predictions at different locations and depths using models trained with different historical data lengths. Each subfigure compares the predictions of MDF-RAGAN, CNN, SITP, and MEAN using training data of 5, 10, and 17 years.

m, 400 m, 1000 m, 1975 m) and four typical shallow and deep sea coordinate points. Overall, the RMSE of MDF-RAGAN shows a continuous decrease at all depths and locations as the length of the training data expands from 5 to 17 years: for example, the RMSE of MDF-RAGAN at a depth of 200 m (point 1: (58.5°S, 19.5°E)) decreases from 0.332 m/s to 0.236 m/s; at the same location at a depth of 1000 m, its error is more than halved from 0.187 m/s to 0.095 m/s. This shows that the longer historical window allows the model to learn a more adequate pattern of thermohaline change, especially in the deep ocean region, where the error decreases more significantly. Further comparing the different depths, it can be seen that the initial RMSE of MDF-RAGAN is higher than that of the deep sea (1000 m, 1975 m) in the shallow sea region (200 m and 400 m), but with the increase of the training years, its error rapidly approaches the deep sea level, and stays in the low range of 0.10-0.20 m/s in all depths at the 17-year window, showing a weak sensitivity to the depth, while the CNN and traditional methods, although performing better in the deep sea, consistently maintain a high amplitude error interval of 0.20-0.95 m/s at shallow depths. In following experiments, the training data length will be 17 years.

Table 1: Comparison of RMSE with different training data lengths

Method	Location	1000 m			1975 m		
		5 years	10 years	17 years	5 years	10 years	17 years
MDF-RAGAN	(58.5°S, 19.5°E)	0.187	0.138	0.125	0.140	0.105	0.095
	(58.5°S, 26.5°E)	0.168	0.151	0.128	0.128	0.114	0.100
	(55.5°S, 22.5°E)	0.226	0.176	0.176	0.168	0.133	0.131
	(52.5°S, 22.5°E)	0.266	0.242	0.245	0.199	0.181	0.182
CNN	(58.5°S, 19.5°E)	0.455	0.460	0.615	0.336	0.341	0.457
	(58.5°S, 26.5°E)	0.545	0.445	0.572	0.408	0.326	0.427
	(55.5°S, 22.5°E)	0.541	0.482	0.661	0.412	0.366	0.501
	(52.5°S, 22.5°E)	0.648	0.542	0.613	0.487	0.410	0.465
SITP	(58.5°S, 19.5°E)	0.437	0.437	0.437	0.319	0.319	0.319
	(58.5°S, 26.5°E)	0.194	0.194	0.194	0.151	0.151	0.151
	(55.5°S, 22.5°E)	0.383	0.383	0.383	0.315	0.315	0.315
	(52.5°S, 22.5°E)	0.385	0.385	0.385	0.357	0.357	0.357
MEAN	(58.5°S, 19.5°E)	0.427	0.427	0.427	0.318	0.318	0.318
	(58.5°S, 26.5°E)	0.219	0.219	0.219	0.164	0.164	0.164
	(55.5°S, 22.5°E)	0.457	0.457	0.457	0.373	0.373	0.373
	(52.5°S, 22.5°E)	0.503	0.503	0.503	0.484	0.484	0.484

Table 2: RMSE comparison of different methods at 1976 m depth across 10 typical locations (data from 2021.01-2023.06)

Number	Location	MDF-RAGAN (m/s)	CNN (m/s)	MEAN (m/s)	SITP (m/s)
1	(58.5°S, 1.5°E)	0.0673	0.3443	0.3120	0.2211
2	(49.5°S, 13.5°E)	0.1191	0.2700	0.3028	0.2050
3	(49.5°S, 16.5°E)	0.1339	0.2902	0.2921	0.1991
4	(49.5°S, 19.5°E)	0.2151	0.3527	0.2891	0.2123
5	(49.5°S, 22.5°E)	0.1877	0.3710	0.3458	0.2883
6	(49.5°S, 31.5°E)	0.0948	0.2203	0.4415	0.3754
7	(46.5°S, 10.5°E)	0.1082	0.2157	0.5471	0.5558
8	(46.5°S, 37.5°E)	0.1543	0.2287	0.2581	0.2016
9	(43.5°S, 22.5°E)	0.2180	0.2762	0.3906	0.3745
10	(43.5°S, 37.5°E)	0.1730	0.3237	0.7380	0.5080
<b>Average</b>		<b>0.1472</b>	<b>0.2893</b>	<b>0.3917</b>	<b>0.3141</b>

### 3.3.2. Accuracy in Deep and Shallow Water

To evaluate the accuracy performance in estimating the SSP, we compare the results of MDF-RAGAN with mean profile, SITP and CNN on 10 typical latitude and longitude coordinate points (30 months of data from 2021.01-2023.06) as shown in Table 2. The results show that the RMSE of the historical average MEAN method fluctuates around 0.25~0.73 m/s, and the RMSE of SITP fluctuates around 0.19~0.55 m/s. While CNN compresses the results to around 0.21~0.37 m/s, the MDF-RAGAN proposed in this paper focuses on 0.06~0.21 m/s, and the mean value is only 0.147 m/s, which is 62% higher than the traditional mean method, and more than 53% compared with the spatial interpolation method. Even compared with CNN, the performance is improved by 49%. The table fully demonstrates the accuracy and stability of MDF-RAGAN for estimation in a large-scale sound velocity gradient environment.

In contrast to the smooth sound velocity variations in the deep-sea region, the SSPs of shallow water bodies tend to show complex nonlinear fluctuations at the thermocline and scattering layer due to strong tidal, wind and internal wave action. Fig. 5 focuses on the estimation results of different methods at 200 m, 400 m, 1000 m, and 1975 m depths at selected shallow sea coordinates. At the 200 m depth section, the prediction curve of the historical averaging method is too flat to reflect the sharp rise of the thermocline due to the complete loss of spatial and temporal information; the inverse distance weighting method introduces the physical neighborhood of the peripheral points, but its fixed power weight limits the flexible response

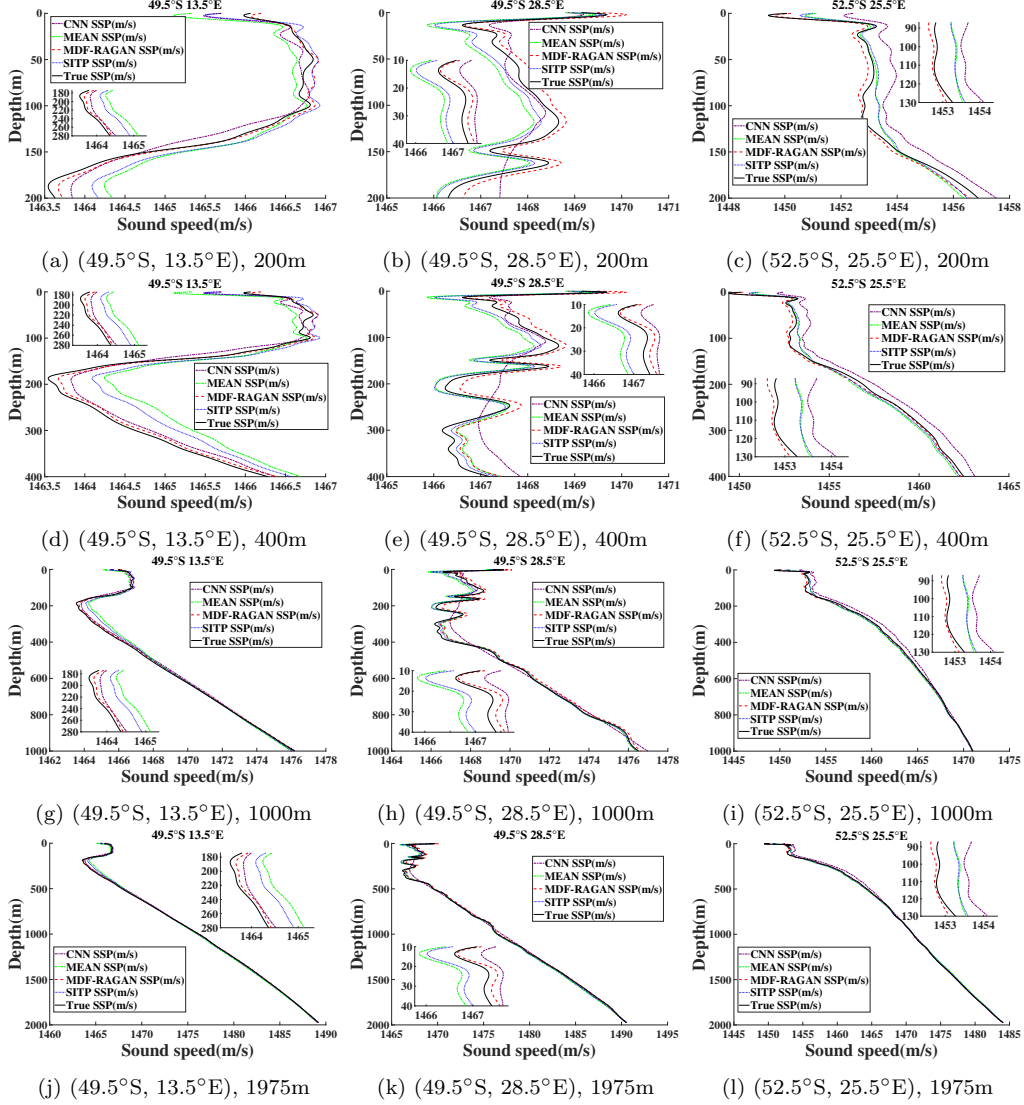


Figure 5: Comparison of sound speed profiles at different locations and depths. Each row represents a specific depth (200 m, 400 m, 1000 m, and 1975 m), while each column represents a specific location (Location 1: (49.5°S, 13.5°E); Location 2: (49.5°S, 28.5°E); Location 3: (52.5°S, 25.5°E)). The figures illustrate the comparison of sound speed profile predictions using four different methods: MDF-RAGAN, CNN, SITP, and MEAN at each location and depth.



to the change of the thermocline amplitude, and thus the predicted peak is often overestimated or underestimated. The CNN is able to capture some of the mutations by the convolution kernel at this depth, but it is not possible to predict the peaks at the depth of 200 m. The CNN is also able to capture some of the mutations at the depth of 400 m by the convolution kernel, but jitters before and after the local extreme points, indicating that the receptive field constructed during its convolution and pooling process does not match the scale of the shallow-sea perturbation.

Table 3: Comparison of RMSE in shallow sea areas at different depths

Method	Location	Depth (m)		
		200	400	1000
MDF-RAGAN	(49.5°S, 16.5°E)	0.2481	0.2191	0.1812
	(49.5°S, 34.5°E)	0.2561	0.2376	0.1280
	(49.5°S, 28.5°E)	0.2641	0.2340	0.2004
	(49.5°S, 31.5°E)	0.1856	0.1666	0.1280
CNN	(49.5°S, 16.5°E)	0.4843	0.4618	0.3971
	(49.5°S, 34.5°E)	0.4346	0.4835	0.2941
	(49.5°S, 28.5°E)	0.4994	0.4754	0.3720
	(49.5°S, 31.5°E)	0.4134	0.3883	0.2941
MEAN	(49.5°S, 16.5°E)	0.3000	0.3239	0.2662
	(49.5°S, 34.5°E)	1.4430	1.5012	0.5114
	(49.5°S, 28.5°E)	0.7325	0.5776	0.4130
	(49.5°S, 31.5°E)	0.9546	0.7745	0.5114
SITP	(49.5°S, 16.5°E)	0.2550	0.2363	0.1848
	(49.5°S, 34.5°E)	1.0823	1.1221	0.4604
	(49.5°S, 28.5°E)	0.5201	0.4192	0.2921
	(49.5°S, 31.5°E)	0.8164	0.6978	0.4604

The shallow sea profile enters the scattering layer at the stage of 200-1000 m. The sound velocity changes in this region are smoother, but there are still small oscillations. Although the errors of MEAN and SITP are slightly reduced, MDF-RAGAN is still much better than the other methods, and the prediction curves of CNN are alleviated at this layer, but it is still difficult to maintain the smoothness at the full depth. In contrast, MDF-RAGAN successfully smoothes out the high-frequency noise and closely follows the measured curves by virtue of the cross-modal attention that dynamically adjusts the fusion weights of the neighborhood and labeled features at each layer of depth. More detailed results at 4 typical locations are given in Table 3.

Overall, MDF-RAGAN’s unified modeling of abrupt and gradual sound speed changes in shallow sea environments is attributed to its multi-source fusion architecture: the LFB provides the coordinates and SST a prior that can constrain the anomaly weights, while the FMB stabilizes the gradients in the depth dimension, allowing the model to adaptively capture perturbed signals in both the thermocline and scattering layers, thus obtaining excellent profile prediction performance under the complex hydrodynamic conditions of shallow seas.

### 3.4. Discussions

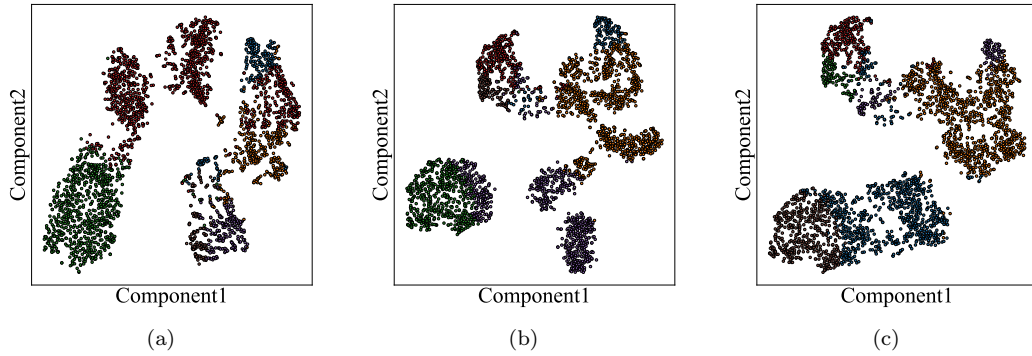


Figure 6: t-SNE visualization of intermediate features in MDF-RAGAN. (a)-(c) show the intermediate features from the discriminator: (a) neighbor label features, (b) target SST-label features, and (c) target LOC-label features.

To evaluate the reconstruction capability of MDF-RAGAN in the feature space, we extracted three types of intermediate embedding features from the discriminator—neighbourhood labels (N-Label), SST labels (T-Label), and coordinate labels (LOC-Label)—and visualised them using t-SNE (Fig.6). Fig.6a shows that the true and generated N-Label samples form clearly separated clusters in the projection space, indicating that multi-source fusion significantly enhances the discriminator’s ability to identify neighbourhood perturbations. The distribution of T-Label features in Fig.6b also exhibits good discriminability, further validating the constraining role of physical priors in the SST channel during adversarial learning. In contrast, the generated distribution of LOC-Label features shown in Fig.6c is almost completely nested within the real sample cluster, indicating that the model has high accuracy and consistency in reconstructing the label space distribution of target points. The above results collectively demonstrate that the cross-modal deep fusion

mechanism implemented by the CMPAB not only enhances the discriminative power of feature representation but also ensures the interpretability and credibility of generated samples in terms of physical semantics. Overall, the distribution structures of the three types of intermediate features systematically validate the effectiveness of MDF-RAGAN in multi-source alignment and local perturbation modelling, providing robust theoretical support and empirical evidence for its application in predicting sound speed profiles in complex marine environments.

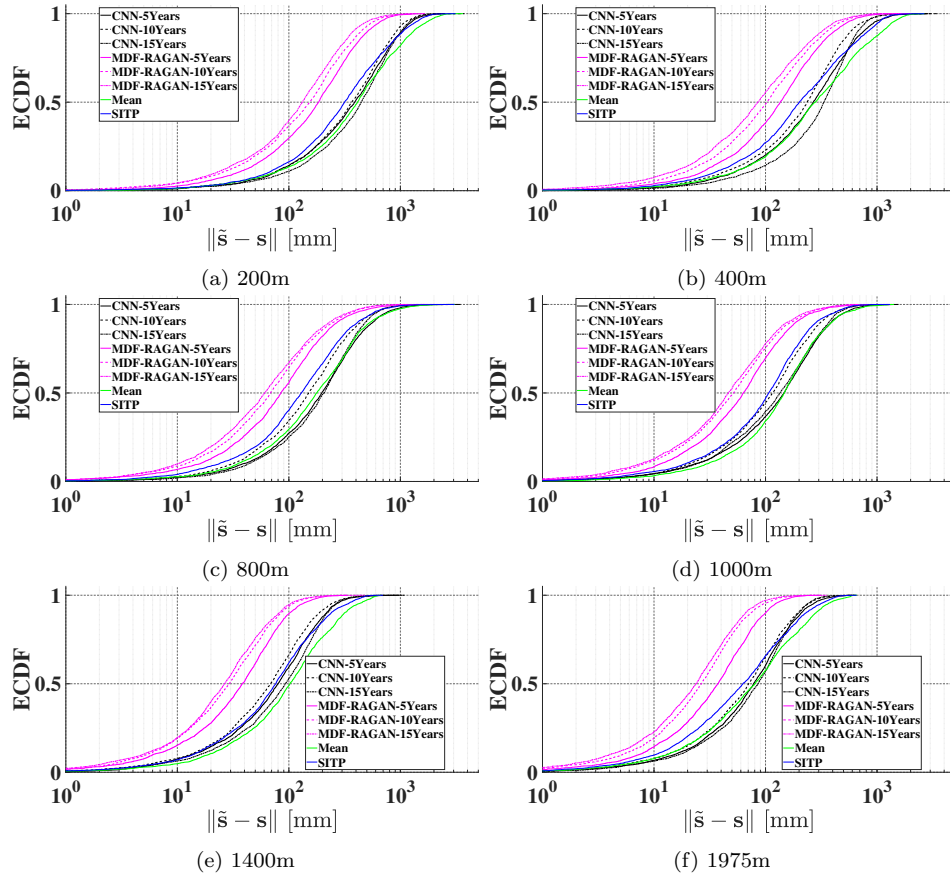


Figure 7: ECDF comparison of absolute prediction errors for different methods at various depths. (a) 200m, (b) 400m, (c) 800m, (d) 1000m, (e) 1400m, (f) 1975m. The curves show that MDF-RAGAN consistently achieves smaller errors and outperforms other baselines across all tested depths.

Although t-SNE visualisation has validated the physical consistency and semantic interpretability of intermediate features in the representation space,

further investigation into the contribution of these learned representations to actual prediction performance remains critical. To this end, we employ empirical cumulative distribution function (ECDF) analysis to assess the absolute prediction error of different methods at various ocean depths. Specifically, we introduce the empirical cumulative distribution function (ECDF) as an evaluation metric to characterise the absolute error distribution of each method at different depths. For each depth layer, we calculate the absolute error between the predicted values and the true values of all samples at that depth point, and plot the cumulative distribution curve of the error magnitude based on this. The horizontal axis of the ECDF curve represents the magnitude of the error (in millimetres), while the vertical axis represents the proportion of samples with errors not exceeding that value.

Firstly, the ECDF curves show the differences in the cumulative distribution of errors between the methods at six typical depth layers (200, 400, 800, 1000, 1400, 1975 m). The ECDF curves for MDF-RAGAN are the most left-shifted and steepest rising in the shallow thermocline layer (200 m vs. 400 m, see Fig. 7a-b): at 200 m depth, about 80% of the samples have an error of less than 50 mm, whereas CNN, SITP, and the mean baseline need to raise the threshold to 200-300 mm to achieve the same hit rate; at 400 m, MDF-RAGAN keeps 90% of the quantile errors within 80 mm, far exceeding the 150-250 mm of the other methods.

Into the middle layer (800 m vs. 1000 m, Fig. 7c-d), the error spectra of all the methods are shifted to the left, but MDF-RAGAN remains ahead of CNN and SITP/MEAN at 80-100 mm with more than 50% of sample errors below 30 mm. In the deeper layers (1400 m vs. 1975 m, Fig. 7e-f), the errors converge further, with MDF-RAGAN achieving a median error of about 20 mm at 1975 m, while CNN is still around 40 mm, and SITP/MEAN is as high as 80-100 mm.

Comparison of the same-coloured solid, dashed and dotted lines in different historical windows (5, 10, 15 years) shows that MDF-RAGAN is the most sensitive to the expansion of the training set, with the ECDF curve shifted left by 10-20 mm. CNN shows only a small improvement, while SITP/MEAN shows few changes, highlighting the advantages of cross-modal attention in enhancing the learning efficiency and generalisation ability of scarce samples.

The comprehensive comparison results based on the whole-profile mean sound speed error (RMSE) are summarized in Table 4. It can be seen that MDF-RAGAN not only outperforms CNN and SITP by nearly a factor of two, but also achieves about 65.8% RMSE reduction compared to MEAN,

which fully reflects the enhancement of overall profile matching by multi-source fusion and cross-modal attention.

Table 4: Comparison of overall RMSE (m/s) across different methods

Methods	RMSE (m/s)	Parameters	Inference Time (ms)
MDF-RAGAN	0.1479	7.7M	4.48
CNN	0.3107	4.69M	0.87
SITP	0.3384	-	-
MEAN	0.4335	-	-

In the shallow sea error analysis, MDF-RAGAN shows lower and more stable RMSE at different depths and spatial locations, with the error fluctuation range of 0.095-0.372 m/s, while CNN and SITP show larger fluctuation in the shallow sea area. Even in the deep sea area where there is a slight convergence, their RMSE remains higher than 0.30 m/s, which is 110% higher than MDF-RAGAN. SITP is limited by the fixed distance weighting and is not adaptive to the dynamic change of depth, with its RMSE being 128% higher. MEAN completely ignores spatial and temporal information and has the largest deviation across the full-profile, with RMSE close to 0.44 m/s. In summary, MDF-RAGAN achieves a comprehensive lead in both point-to-point and distribution-level evaluation metrics, reflecting the comprehensive superiority of the proposed model in the sound speed profile prediction task.

#### 4. Conclusion

To realize high-precision estimation of sound velocity distribution in a given sea area without on-site underwater data measurement, we propose the MDF-RAGAN model for SSP construction. The attention mechanism is embedded to improve the model’s ability for capturing global spatial feature correlations, and the residual module is embedded for deeply capturing small disturbances in the deep ocean sound velocity distribution caused by changes of SST. Through experiments on real open dataset, it shows that the proposed model outperforms other state-of-the-art methods. Specifically, MDF-RAGAN not only outperforms CNN and SITP by nearly a factor of two, but also achieves about 65.8% RMSE reduction compared to MEAN, which fully reflects the enhancement of overall profile matching by multi-source fusion and cross-modal attention.

## References

- Bianco, M., Gerstoft, P., 2017. Dictionary learning of sound speed profiles. *The Journal of the Acoustical Society of America* 140, 1749–1758.
- Choo, Y., Seong, W., 2018. Compressive sound speed profile inversion using beamforming results. *Remote Sensing* 10, 1–18. doi:10.3390/rs10050704.
- Erol-Kantarci, M., Mouftah, H.T., Oktug, S., 2011. A survey of architectures and localization techniques for underwater acoustic sensor networks. *IEEE Communications Surveys & Tutorials* 13, 487–502. doi:10.1109/SURV.2011.020211.00035.
- Huang, B., Liu, C., Banzon, V., Freeman, E., Graham, G., Hankins, B., Smith, T., Zhang, H.M., 2021a. Improvements of the daily optimum interpolation sea surface temperature (doisst) version 2.1. *Journal of Climate* 34, 2923 – 2939. URL: <https://journals.ametsoc.org/view/journals/clim/34/8/JCLI-D-20-0166.1.xml>, doi:10.1175/JCLI-D-20-0166.1.
- Huang, W., Li, D., Zhang, H., Xu, T., Yin, F., 2023. A meta-deep-learning framework for spatio-temporal underwater ssp inversion. *Frontiers in Marine Science* 10, 1–22. doi:10.3389/fmars.2023.1146333.
- Huang, W., Liu, M., Li, D., Yin, F., Chen, H., Zhou, J., Xu, H., 2021b. Collaborating ray tracing and ai model for auv-assisted 3-d underwater sound-speed inversion. *IEEE Journal of Oceanic Engineering* 46, 1372–1390.
- Li, F., Zhang, R., 2010. Inversion for sound speed profile by using a bottom mounted horizontal line array in shallow water. *Chinese Physics Letters* 27, 084303:1–4. doi:10.1088/0256-307X/27/8/084303.
- Li, H., Qu, K., Zhou, J., Aug., 2021. Reconstructing sound speed profile from remote sensing data: Nonlinear inversion based on self-organizing map. *IEEE Access* 9, 109754–109762. doi:10.1109/ACCESS.2021.3102608.
- Li Hong, Xu Fanghua, e.a., 2017. Development of a global gridded argo data set with barnes successive corrections. *Journal of Geophysical Research:Oceans* 122, 866–889.

- Lu, J., Huang, W., Zhang, H., Jan., 2024. Dynamic prediction of full-ocean depth ssp by a hierarchical lstm: An experimental result. *IEEE Geosci. Remote Sens. Lett.* 21, 1–5. doi:10.1109/LGRS.2024.3356552.
- Luo, J., Yang, Y., Wang, Z., Chen, Y., 2021. Localization algorithm for underwater sensor network: A review. *IEEE Internet of Things Journal* 8, 13126–13144. doi:10.1109/JIOT.2021.3081918.
- Piao, S., Yan, X., Li, Q., Li, Z., Wang, Z., Zhu, J., 2023. Time series prediction of shallow water sound speed profile in the presence of internal solitary wave trains. *Ocean Engineering* 283, 115058. doi:10.1016/j.oceaneng.2023.115058.
- Piccolo, J., Haramuniz, G., Michalopoulou, Z.H., 2019. Geoacoustic inversion with generalized additive models. *The Journal of the Acoustical Society of America* 145, 463–468.
- Stephan, Y., Thiria, S., Badran, F., 1995. Inverting tomographic data with neural nets, in: 'Challenges of Our Changing Global Environment'. Conference Proceedings. OCEANS'95 MTS/IEEE, IEEE. pp. 1501–1504. doi:10.1109/OCEANS.1995.528711.
- Tolstoy, A., Diachok, O., Frazer, L., 1991. Acoustic tomography via matched field processing. *The Journal of the Acoustical Society of America* 89, 1119–1127. doi:10.1121/1.400647.
- Wang, Y., Cai, W., Weng, D., Sheng, Q., 2014. A sbe-19plus based real-time monitoring system of ctd data, in: OCEANS 2014 - TAIPEI, pp. 1–4.
- Wu, P., Zhang, H., Shi, Y., Lu, J., Li, S., Huang, W., Tang, N., Wang, S., 2024. Real-time estimation of underwater sound speed profiles with a data fusion convolutional neural network model. *Applied Ocean Research* 150, 104088. URL: <https://www.sciencedirect.com/science/article/pii/S0141118724002098>, doi:<https://doi.org/10.1016/j.apor.2024.104088>.
- Zhang, M., Xu, W., Xu, Y., 2015. Inversion of the sound speed with radiated noise of an autonomous underwater vehicle in shallow water waveguides. *IEEE Journal of Oceanic Engineering* 41, 204–216. doi:10.1109/JOE.2015.2418172.

Zhang, W., Yang, S.e., Huang, Y.w., Li, L., 2012. Inversion of sound speed profile in shallow water with irregular seabed, in: Advances in Ocean Acoustics: Proceedings of the 3rd International Conference on Ocean Acoustics (OA2012), AIP. pp. 392–399. doi:10.1063/1.4765934.